On the Formation of Whitecaps by a Threshold Mechanism. Part III: Field Experiment and Comparison with Theory

R. L. SNYDER, LINDA SMITH AND R. M. KENNEDY

Nova University, Dania, FL 33004

(Manuscript received 19 April 1980, in final form 9 May 1983)

ABSTRACT

This paper is the third in a series of papers which seek to evaluate the hypothesis that deep water whitecapping is predictable in terms of a threshold mechanism involving the vertical acceleration. Parts I and II of the series have developed the descriptive framework for the investigation and examined several geometrostatistical predictions of the threshold model, the first by direct integration of the joint probability densities for the vertical acceleration, the second by Monte Carlo simulation of the vertical acceleration field.

In Part III we describe a field experiment designed to study the statistical geometry of the whitecap field and to test the theoretical predictions of Parts I and II. This experiment, conducted at an experimental site in the Bight of Abaco, Bahamas, combines a series of photographs of whitecap events with simultaneous array measurements of waves. The photographs were taken from above the water surface and cover an area nominally 10 m on a side. A total of 2292 whitecap events (~10 000 frames), obtained in winds to 10 m s^{-1}, were analyzed.

Using the technique of Snyder and Smith, the vertical acceleration field was estimated in the vicinity of selected whitecap events (from the recorded signals of a 7-component wave recorder array in the field-of-view of the camera). Statistical allowance for the contribution of higher frequency wave components not included in the analysis suggests that the observed accelerations are consistent with a vertical acceleration threshold of approximately $0.5g$.

Statistical analysis of all observed events produces a probability of breaking and moment statistics which are likewise reasonably consistent, though not uniformly so, with the theoretical predictions of Parts I and II.

We conclude that to some level of approximation the vertical acceleration threshold model may indeed predict whitecapping. The appropriate threshold level appears to be approximately $0.5g$. This conclusion is less than definitive because our analysis is limited to wave components with frequencies less than twice the frequency of the spectral peak.

1. Introduction

Design of an appropriate and practical field experiment to study the geometry and geometrical statistics of the whitecap field is difficult for several reasons:

1) Whitecaps are comparatively rare and fleeting events. Although the probability that a photograph taken at random will contain breaking water is directly proportional to the surface area covered by the photograph, there are practical limits to the area which can be monitored from a platform which is not airborne. We anticipate that for such a platform the probability that a random photograph will contain breaking water will be small. (For the experiments described here, this probability was typically of order one in fifty.)

2) An important implication of the threshold model is that the whitecapping mechanism depends upon the wave field over a wide range of frequencies. The instrumentation necessary to adequately monitor the wave field over such a range is elaborate (and considerably beyond our means).

We have dealt with the first problem by triggering our camera with the sound of breaking water within and close by its field of view. This procedure reduces the proportion of waste frames to an acceptable limit (roughly ½ to ⅔ of all frames). At the same time, however, it eliminates roughly the first ⅛ second of each whitecap from the photographic record, and introduces a minimum whitecap size below which there is no photographic record.

Our solution to the second problem is less satisfactory. Consistent with the scaling hypothesis introduced in Part I, we do what we can to monitor the wave field over a restricted range of frequency. However, this range is more restricted than we would like (It does not match the cutoff implied by the size of the smallest whitecap which triggers the camera.), and our efforts here are further degraded by the use of less than optimum wave recorders (strain gauges) and by a number of other instrumental difficulties.

Nonetheless, our measurements provide an estimate of the directional spectrum for frequencies to twice the peak frequency. Also, because the array is situated in the field-of-view of the camera, these measurements allow a partial reconstruction of the gravity wave contribution to the vertical acceleration field in regions of active breaking. Thus two comparisons with the threshold model are possible, 1) a direct evaluation of the partial vertical acceleration level in whitecaps, and 2) a comparison of observed statistics with those predicted in Parts I and II of this series.

In the next section we describe the instrumentation and field experiment. Section 3 deals with the analysis of wave data, and Section 4 with the reduction of the whitecap photographs. The reconstruction of the vertical acceleration field in the neighborhood of selected whitecap events is discussed in Section 5, and the observed whitecap statistics are presented in Section 6. Finally in Section 7 we summarize the findings of our three-part study.

2. Field experiment

The site of the field experiment was the same Bahama Bank site employed in several recent studies of fluctuations of atmospheric pressure above the water surface (Snyder, 1974; Snyder *et al.*, 1979). This site is in the Bight of Abaco, 5 km south of Black Point, Little Abaco (Fig. 1). Several features of the site make it ideal for surface gravity wave studies. Its 7 m depth is convenient for horizontal array measurements (the bottom can be used as a platform to support instrumentation); its enclosed geometry ensures a fetch limited sea (dimensionless fetch typically varies from 10^3 to 10^4, depending on wind speed and direction); weather conditions are moderate and relatively predictable.

It was with a view towards the whitecap project that a site tower was originally erected in 1966. This tower, a stayed 13 cm diameter pipe supporting a small work platform, projects some 5 m above the water surface. Mounted on the tower is a 13 m boom free to orient into the wind. The camera, a 35 mm pulsed Neyhart Automax G2 with data box, is located at the upwind end of the boom and looks down over a square patch of water surface nominally 10 m on a side. In addition to rotating azimuthally, the boom swings up and down; this allows the removal of the camera to a 13′ Boston Whaler in order to reload film (an operation possible in winds to 10 m s^{-1}). An acoustic antenna, consisting of a microphone and defocussed parabolic reflector, is located on the boom at some distance from the camera (to avoid acoustic feedback from the camera). The field-of-view of this antenna roughly matches that of the camera.

Analysis of tape recordings of the noise generated by whitecaps shows a broad peak in the band 2–5 KHz. We trigger the camera (pulsed at the rate of 8 frames per second) for as long as the noise in this band remains above some trigger level. (In fact the camera is programmed to take pictures for ¼ s after the noise falls below this level.) The trigger level is set in the field so as to minimize false triggers from whitecaps outside the field-of-view of the camera without losing too many of the smaller whitecaps occurring within this field-of-view.

In addition to the camera and microphone, the tower supports a Taylor anemometer, azimuth pot (linked to the boom), and step-resistance tide gauge (D. G. Hunley, unpublished). A wave recorder array is located SE of the tower (Fig. 2). During the first of two experiments in April 1968, this array contained four Snodgrass Mark X pressure transducers. During the second experiment in December 1972, these instruments were augmented by three specially constructed step-resistance wave staffs with a range

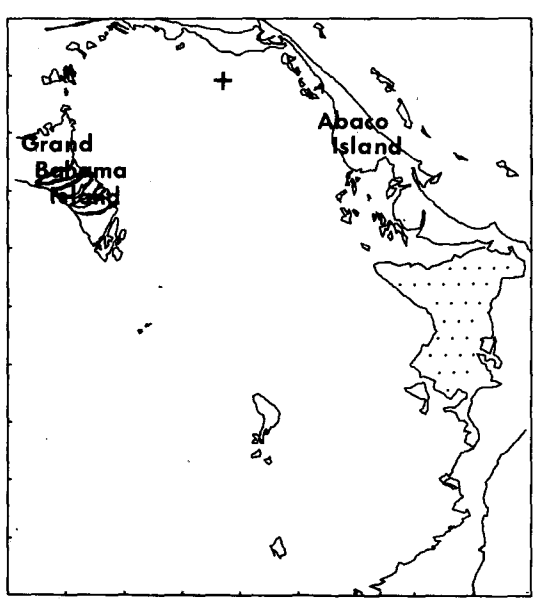

FIG. 1. Bight of Abaco experimental site (cross near top). Stippled area is a mangrove swamp. Bank region between the islands has a maximum depth of 10 m. Scale is 10 km per division.

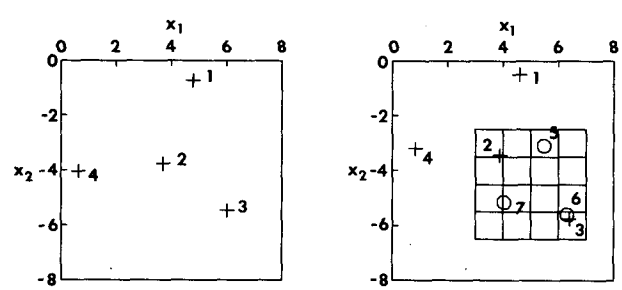

FIG. 2. Instrument configurations for the 1968 and 1972 experiments. Instruments 1–4 (crosses) are Snodgrass Mark X wave gauges; instruments 5–7 (open circles) are step resistance wave staffs.

of 1.6 m and a resolution of 0.006 m (D. G. Hunley, unpublished). These staffs, introduced to improve the small scale resolving power of the array, were only partially successful. A contamination problem, which had not appeared in pre-experiment tests away from the Bight, resulted in significant loss of signal within 30 minutes of immersion. To overcome this difficulty the second experiment was run in 10 minute increments, wiping the staffs clean prior to each increment.

As in other Bight experiments the wave data were acquired aboard a small research vessel using a 16-channel digital data acquisition system (Radiation, Inc. Model 5015). The vessel (R/V *Gerda*, R/V *Gulfstream*) was moored 100 m west of the tower and connected to the tower instrumentation by cables on the bottom. Several other signals were also acquired on this system: wind speed (December experiment only), wind direction, audio level (rectified and low passed), and trigger signal. Mean water level, wind direction, and wind speed were simultaneously recorded on Rustrak recorders.

During the April experiment nineteen films were exposed, of which eleven were eventually digitized. All of the digitized films (nominally 1600 frames long) were taken with Plus X film using a red filter to enhance the contrast between whitecaps and background. During the December experiment nine films (all Plus X) were exposed, all of which were at least partially digitized. (Films 4 and 6 were digitized only for events occurring near the wave staffs.) A run summary for all digitized films (both experiments) is given in Table 1.

TABLE 1. Run summary.

Run number	Film number	T (s)	W (m s^{-1})	ϑ_W (rad)	D (m s^{-1})	ϑ_D (rad)	α	Ω (rad s^{-1})	γ	σ	Θ (rad)	ζ_{rms} (m)	λ_{rms} (m s^{-2})	Remarks
4–5	2	2705	6.79	3.27	0.18	2.75	0.0205	2.58	—	—	−3.13	0.093	0.97	
6–7	3	2280	7.01	−2.95	0.16	−3.06	0.0233	2.47	—	—	3.10	0.095	1.00	
8–9	4	1560	7.60	−2.99	0.12	−3.05	0.0230	2.37	—	—	3.03	0.100	1.02	
45–46	13	1020	2.84	2.21	0.12	2.08	0.0052	2.15	—	—	1.91	0.059	0.49	no whitecaps
51–52	13	1425	1.04	2.02	0.09	1.97	0.0038	2.17	—	—	1.86	0.053	0.44	no whitecaps
53	13	3240	5.66	−2.95	0.12	−3.07	0.0198	2.65	—	—	3.07	0.084	0.96	
55	15	1955	4.65	3.09	0.16	−2.98	0.0237	2.71	—	—	2.84	0.078	0.97	only part
56	16	1680	4.99	2.34	0.12	2.39	0.0094	2.18	—	—	1.94	0.087	0.69	
57	17	6720	2.75	1.83	0.09	2.49	0.0066	2.16	—	—	1.88	0.074	0.58	
58–59	17	3360	4.60	2.13	0.17	2.76	0.0166	2.38	—	—	1.81	0.085	0.83	
60–61	18	7145	4.14	1.72	0.10	2.36	0.0100	2.24	—	—	1.73	0.069	0.66	only part
62	19	3060	6.43	1.13	0.09	1.26	0.0153	2.42	—	—	1.52	0.086	0.85	
3	1	3000	5.80	3.02	0.17	2.99	0.0080	2.45	1.83	0.14	2.59	0.074	0.70	
4	1	1320	6.19	−3.10	0.17	−3.03	0.0124	2.63	—	—	2.69	0.074	0.81	
5	2	1200	6.99	3.12	0.22	−3.04	0.0117	2.45	2.43	0.11	2.91	0.091	0.82	
6	2	960	6.53	3.13	0.21	−3.11	0.0100	2.35	—	—	2.83	0.091	0.79	
7	3	720	7.43	−3.02	0.15	2.94	0.0131	2.38	—	—	2.90	0.093	0.85	
8	3	540	7.70	−3.06	0.18	−2.82	0.0210	2.51	—	—	2.93	0.114	1.08	
9	4	840	6.38	2.16	0.06	2.54	0.0117	2.36	1.93	0.09	2.79	0.089	0.80	*
10	4	600	6.32	2.17	0.13	2.72	0.0110	2.44	2.05	0.13	2.75	0.090	0.82	*
11	4	955	5.69	2.16	0.13	2.61	0.0086	2.31	—	—	2.73	0.087	0.72	*
12	4	1090	5.72	2.16	0.11	3.01	0.0095	2.32	—	—	2.76	0.085	0.71	*
13	5	600	6.85	2.59	0.13	3.06	0.0076	2.30	3.72	0.16	2.55	0.101	0.73	
14	5	570	6.80	2.75	0.09	−2.94	0.0097	2.19	2.30	0.09	2.55	0.099	0.74	
15	5	260	6.63	2.74	0.08	2.98	0.0080	2.08	3.00	0.09	2.46	0.105	0.73	
23	6	960	6.01	2.40	0.14	2.68	0.0121	2.60	—	—	3.03	0.075	0.81	*
24	6	990	6.19	2.41	0.12	−3.06	0.0121	2.58	—	—	3.05	0.077	0.80	*
25	6	770	6.35	2.40	0.12	2.89	0.0100	2.53	2.24	0.09	3.05	0.076	0.77	*
26	7	865	6.35	2.05	0.11	−3.04	0.0089	2.41	—	—	2.98	0.081	0.73	
27	7	735	6.56	2.05	0.09	3.11	0.0169	2.42	2.11	0.08	3.00	0.084	0.77	
28	7	1105	6.28	2.04	0.14	−2.77	0.0089	2.45	2.83	0.12	2.95	0.085	0.76	
29	8	620	8.32	2.09	0.13	2.21	0.0103	2.13	—	—	2.71	0.131	0.87	
30	8	390	8.95	2.10	0.16	2.58	0.0075	2.02	—	—	2.71	0.143	0.80	
31	9	635	5.78	2.28	0.14	2.52	0.0071	2.36	2.51	0.09	2.70	0.077	0.70	squall
32	9	960	4.31	2.33	0.13	2.31	0.0096	2.36	2.26	0.10	2.80	0.085	0.77	
33	9	1050	6.90	2.38	0.13	2.99	0.0103	2.60	—	—	2.90	0.062	0.73	
34	9	780	6.60	2.38	0.11	2.96	0.0106	2.60	—	—	2.95	0.077	0.79	
35	9	830	6.61	2.37	0.12	−2.82	0.0119	2.56	—	—	3.00	0.079	0.82	
36	9	720	6.29	2.36	0.12	2.68	0.0108	2.55	2.46	0.14	2.99	0.084	0.79	

* Only whitecaps near wave staffs digitized.

3. Analysis of wave data

In order to obtain a unified description of the wave data, we introduce the field variable

$$Z(\mathbf{x}, z, t) \equiv \frac{1}{\rho g} P(\mathbf{x}, z, t),$$

where P is the pressure and Z is a kind of generalized surface elevation which decays exponentially away from the surface and is equal to the surface elevation for $z = 0$ (linear theory). Thus, both the pressure gauges and the wave staff provide direct estimates for Z (at different z) and may be discussed in terms of these estimates.

The estimates for Z from each run were Fourier analyzed and cross-spectra were computed for all instrument pairs, using a Bartlett (1950) procedure with Lanczos squared data window. The statistical reliability of the resulting estimates varies with the length of run; estimates for the 10 minute runs of the December 1972 experiment have ~40 degrees of freedom. These cross-spectral estimates, corrected for instrument response, constitute the principal data to be fit by the directional spectrum analysis.

Comparison of autospectral values among and between pressure gauges and wave staffs (December experiment) reveals a number of problems with the wave data:

1) The disagreement among pressure gauge autospectra is typically somewhat larger than implied by statistical considerations.
2) The disagreement among wave staff autospectra is likewise typically somewhat larger than implied by statistical considerations.
3) The ratio between wave staff and pressure gauge autospectra is larger than would be expected from the measured elevations of the pressure gauge probes.

The discrepancies inherent in the first two problems are relatively small (generally less than 15% at the spectral level), and so we have simply ignored them—except to throw out an occasional record. The third problem requires a correction. Somewhat arbitrarily, we assume that during the December experiment the pressure gauges were one foot lower in the water column than indicated by our vertical survey. Had we chosen instead to make a direct loss of signal correction (due to contact resistance in the underwater connections) we would undoubtedly achieve very similar results near the spectral peak, with significant differences apparent only at higher frequencies. Nevertheless, the uncertainty over the pressure gauge correction underscores our inability to reliably carry the analysis of present data much beyond twice the peak frequency.

The directional spectrum analysis of the wave data is similar to that described by Snyder *et al.* (1981). This analysis exploits the relationship linking the cross-spectrum between two wave recorders $G_{Z^2}(\boldsymbol{\xi}, z_1, z_2, \omega)$ to the directional wave spectrum $E_{\xi^2}(\omega, \vartheta)$

$$G_{Z^2} = \int d\vartheta E_{\xi^2} e^{|\mathbf{k}|(z_1+z_2)} e^{-i\mathbf{k}\cdot\boldsymbol{\xi}}, \quad \omega > 0, \qquad (1)$$

with a similar expression for $\omega < 0$. Here $\boldsymbol{\xi}$ is the horizontal displacement of the wave recorders, $\boldsymbol{\xi} \equiv \mathbf{x}_2 - \mathbf{x}_1$, z_1 and z_2 are their vertical elevations relative to the mean surface (for the wave staffs $z = 0$), and $\mathbf{k}(\omega, \vartheta, \mathbf{D})$ is the vector wavenumber associated with the (ω, ϑ) component, given the "effective" drift $\mathbf{D}$ (here assumed constant).

We expand $E_{\xi^2}(\omega, \vartheta)$ in the form

$$E_{\xi^2}(\omega, \vartheta) = \sum_n^N {}_nE_{\xi^2}(\omega)\psi_n(\vartheta - \vartheta_w), \quad \text{linear analysis}$$

or

$$E_{\xi^2}(\omega, \vartheta) = [\sum_n^N {}_nE_{\xi^2}(\omega)\psi_n(\vartheta - \vartheta_w)]^2, \quad \text{bilinear analysis}$$

where ϑ_w is the wind azimuth, and where $\psi_n(\vartheta)$ is given by

$$\psi_n(\vartheta) \equiv \cos\frac{3}{4}\vartheta \cos\frac{3}{4}(n-1)\vartheta, \quad |\vartheta| \leqslant \frac{4\pi}{3}, \quad n \text{ odd},$$

$$\equiv \cos\frac{3}{4}\vartheta \sin\frac{3}{4}n\vartheta, \quad |\vartheta| \leqslant \frac{4\pi}{3}, \quad n \text{ even},$$

$$\equiv 0, \quad |\vartheta| > \frac{4\pi}{3}.$$

This choice for $\psi_n(\vartheta)$ ensures that wave components whose direction of travel differs from the wind direction by more than 120° do not contribute to the spectrum. In the bilinear case the resulting spectrum is everywhere $\geqslant 0$.

We then fix the unknowns ${}_nE_{\xi^2}(\omega)$, $n = 1, 2, \ldots, N$ and $\mathbf{D}$ by minimizing the variances

$$V(\omega) \equiv \sum_{jk} |G_{jk}(\omega) - G_{Z^2}(\boldsymbol{\xi}_{jk}, z_j, z_k, \omega)|^2$$

and

$$V \equiv \int d\omega V(\omega),$$

respectively, where $G_{jk}(\omega)$ is the observed cross spectrum between the jth and kth instruments. These minimizations are repeated until both the ${}_nE_{\xi^2}$ and $\mathbf{D}$ have converged (typically three or four iterations). The first two iterations employ the linear form for E_{ξ^2}; subsequent iterations employ the bilinear form.

The resulting directional spectrum for runs 13, 14, 15 from December 1972 is displayed in Fig. 3. Note the characteristic shift in peak direction with frequency resulting from the nonuniform fetch distribution. Also note the tendency for the directional spread to increase with frequency.

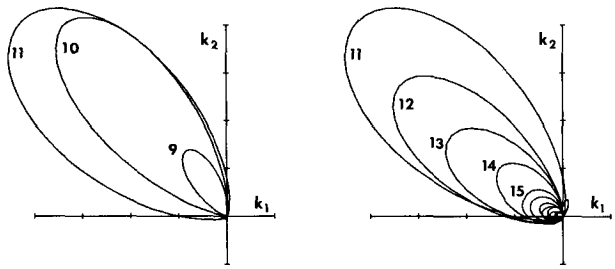

FIG. 3. Directional spectrum. Bands 9–11 and 11–22, run 13–15. Frequency interval is 0.196 rad s^{-1}. Scale is 0.002 m^2 s per division.

The directional spectrum analysis was followed by two analyses designed to characterize the resulting spectra in terms of a set of bulk parameters. In the first of these we compute the spectral moments

$$m_{jk} \equiv \int d\omega \int d\theta(\omega \cos\vartheta)^j(\omega \sin\vartheta)^k E_{\zeta^2}.$$

The integral runs over all ϑ and to twice the peak frequency. The derived parameters

$$J_{\text{rms}} \equiv (m_{00})^{1/2},$$

$$\Theta \equiv \tan^{-1}\left(\frac{m_{01}}{m_{10}}\right),$$

$$\lambda_{\text{rms}} \equiv (m_{04} + 2m_{22} + m_{40})^{1/2}$$

representing the rms surface elevation, a characteristic frequency and the rms vertical acceleration are shown in the run summary, Table 1.

Also shown in this table are the parameters α, Ω, γ, and σ resulting from the second analysis, a nonlinear fit of the integrated spectrum

$$\int d\vartheta E_{\zeta^2}(\omega, \vartheta)$$

to the JONSWAP form (Hasselmann, *et al.*, 1973)

$$D_{\zeta^2}(\omega) \equiv \alpha g^2 \omega^{-5} e^{-\frac{5}{4}\left(\frac{\Omega}{\omega}\right)^4} \gamma^{e^{-\frac{(\omega-\Omega)^2}{2\sigma^2\Omega^1}}}.$$

4. Reduction of whitecap photographs

Figure 4 shows a whitecap photograph from one of the December 1972 runs. Visible in the photograph are a whitecap, residual foam, sun glitter, a pair of tower stays with fiducial marks (only one fiducial is apparent), and several step-resistance wave staffs; also photographed are accutron time, frame count, and film identification.

Some difficulty is typically encountered in distinguishing between active breaking, residual foam, and sun glitter; however, it is usually possible to make this distinction. Residual foam is relatively shortlived

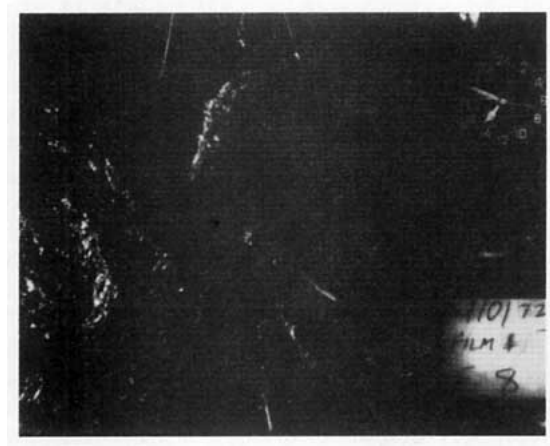

FIG. 4. Whitecap photograph. Frame 9, event 9, run 26, 1972.

(several frame intervals) and typically somewhat disconnected. It is upwind of the active breaking. (In the photograph shown, the tower boom has been constrained so that the wind is from the lower right corner.) Sun glitter is sharply defined and high contrast. It is typically confined to certain portions of the field of view.

The photographs are scanned with a viewing table built by D. G. Hunley, employing a photocell and two multi-turn potentiometers, driven by racks. The scanned photographs are corrected for background light level (as a function of position), converted to digital images and filed on disk. The resulting images constitute the data base for the analysis which follows. Figure 5 shows the computer image of the whitecap of Fig. 4.

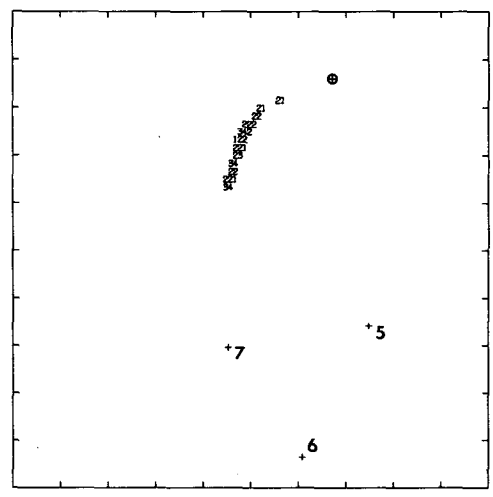

FIG. 5. Computer image of Frame 9, event 9, run 26, 1972. Display shows average log light intensity level relative to background at various parts of whitecap. Also shown are the locations of the three wave staffs and of one (of two) stay fiducials. Scale is 0.1395 grid units per division.

The remaining tasks in the reduction of the whitecap photographs are to determine a precise registration in both time and space for each photograph and to group the photographs into a series of whitecap events. Rough registrations may be computed from the accutron time recorded in the photographs (readable to 1 second, accurate to several seconds) and from the corresponding boom azimuth (resulting in a position accuracy of perhaps 0.5 m). The reconstruction effort of the next section, however, requires order of magnitude better registrations.

To determine a precise standard time for each photograph we compare the photographic record with the trigger signal recorded by the data acquisition system. Each positive section of the trigger signal corresponds to a series of overlapping whitecap events (usually a single event) some occurring within the field-of-view of the camera, others occurring outside this field-of-view. Using an approximate time derived from the accutron time, we determine the correspondence between such "aggregate" events in the trigger signal and those defined by the photographic record. We then assign to the first frame of each aggregate event an improved time equal to the start time of the corresponding aggregate event in the trigger signal. Improved times for subsequent frames are computed by incrementing this start time in steps of ⅛ s. Figure 6 shows the resulting correspondence of aggregate events for run 14 from December 1972.

The digitization of whitecap photographs employs a spatial reference frame which imagines the object plane to be at unit distance from the camera. (Calibration of the viewing table co-range coordinates with respect to this frame is accomplished by scanning a rectangular grid prior to the digitization of each film.) To estimate the true horizontal coordinates of a point in the object plane we employ the algorithm

$$\begin{bmatrix} x_1 \\ x_2 \end{bmatrix} = z_c \begin{bmatrix} \sin(\varphi - \psi) & \cos(\varphi - \psi) \\ -\cos(\varphi - \psi) & \sin(\varphi - \psi) \end{bmatrix} \begin{bmatrix} y_1 \\ y_2 \end{bmatrix} - R \begin{bmatrix} \cos\psi \\ \sin\varphi \end{bmatrix}.$$

Here x is the true position of the point and y its reference position, z_c is the elevation of the camera relative to the mean surface, R its radius of swing, and φ is the aximuth of the boom (travel towards, counterclockwise from east). The origin of the x frame is in the tower with the x_1 axis towards the east.

Because the azimuth potentiometer yields only a rough value for φ, this value was improved, frame by frame, by inverting the above algorithm and fitting the reference coordinates of the stay fiducials and wave staffs to their observed values. Simultaneously the camera rotation parameter ψ and "effective" swing radius R were determined by a bulk analysis of 100 frames from December 1972 (an iterative fit involving alternate computations of the φ's). This fit yields $R = 4.77$ m and $\psi = 2.5°$ with a standard deviation of 0.06 m (the precision of the resulting spatial registration). The effective swing radius compares with a nominal value of 4.86 m and corresponds to an inward tilt of 0.7°. (We note that the above algorithm does not completely account for tilt, only for the translation inherent in this tilt near the center of the field of view. Because the tilt was small, we felt that the complications of a more complete correction did not justify its implementation.)

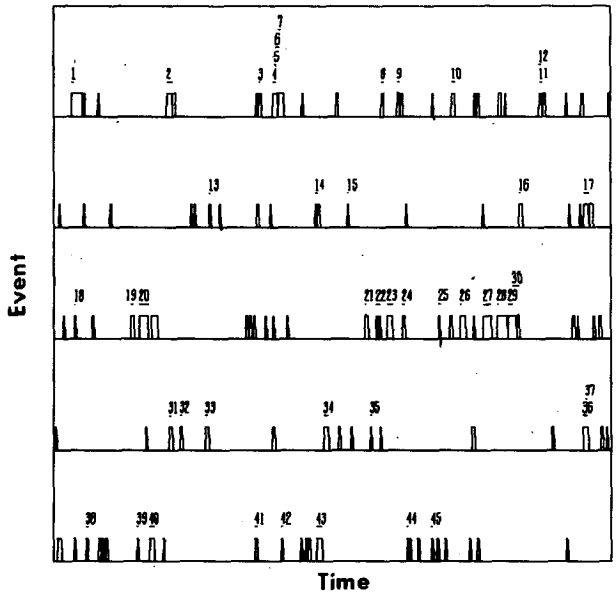

FIG. 6. Event summary, run 14, December 1972. Summary is divided into five 2-minute intervals, running top to bottom, left to right. Shown are the trigger signal (including events outside the field of view of the camera) and the time registered photographic record (events 1–45).

5. Reconstruction of the vertical acceleration field

The deployment of a wave recorder array in the field-of-view of the camera makes possible the experimental determination of partial vertical acceleration levels in and around regions of active breaking. Following Snyder and Smith (1973), we seek an optimum set of weight functions ${}_nK_{\lambda Z}$ such that the sum

$$\lambda'(\mathbf{x}, t) = \sum_n^N \int_{-\infty}^{\infty} d\tau\, {}_nK_{\lambda Z}(\mathbf{x}, t - \tau) Z(\mathbf{x}_n, z_n, \tau)$$

best approximates the field variable $\lambda(\mathbf{x}, t)$. We are given the directional wave spectrum $E_{\zeta^2}(\omega, \vartheta)$ and the N wave records

$$Z(\mathbf{x}_n, z_n, t), \quad n = 1, 2, \ldots, N.$$

As shown by Snyder and Smith, the Fourier transforms

$${}_nH_{\lambda Z}(\mathbf{x}, \omega) \equiv \frac{1}{2\pi} \int_{-\infty}^{\infty} d\tau\, {}_nK_{\lambda Z}(\mathbf{x}, \tau) e^{-i\omega\tau}$$

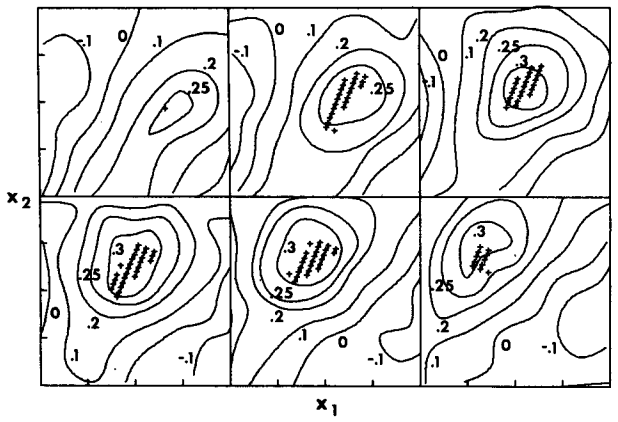

FIG. 7. Threshold variable contours (in units of g). Event 48, film 5, 1972. Sequence is from top to bottom, left to right. Time interval is 0.125 s. Crosses show location of breaking water. Horizontal scale is 1 m per division.

are determined by the relations

$$\sum_{m}^{N} G_{Z^2}(\mathbf{x}_n - \mathbf{x}_m, z_m, z_n, \omega)_m H_{\lambda Z}(\mathbf{x}, \omega) = \frac{1}{2\pi} G_{\lambda Z}(\mathbf{x} - \mathbf{x}_n, z_n, \omega), \quad n = 1, 2, \ldots, N,$$

where

$$G_{\lambda Z}(\xi, z, \omega) \equiv \omega^2 \int_0^{2\pi} d\vartheta E_{\zeta^2}(\omega, \vartheta) e^{|\mathbf{k}|z} e^{-i\mathbf{k}\cdot\xi}, \quad \omega > 0$$

and

$$G_{Z^2}(\xi, z_1, z_2, \omega) \equiv \int_0^{2\pi} d\vartheta E_{\zeta^2}(\omega, \vartheta) e^{|\mathbf{k}|(z_1+z_2)} e^{-i\mathbf{k}\cdot\xi}, \quad \omega > 0$$

with similar relations for $\omega < 0$. We note that the formalism allows for an effective mean current $\mathbf{D}(\omega, \vartheta)$, which enters the computation through the vector wavenumber $\mathbf{k}$.

The December 1972 whitecap photographs were screened for events occurring in and near the wave staff portion of the wave recorder array. A total of 26 events were chosen for analysis. In each case the partial vertical acceleration was estimated at each point of a five-by-five grid (shown in Fig. 2) for a 32 s period centered on the whitecap event. These estimates were based on the bilinear directional spectra computed in Section 3 (with drift) and typically six of seven wave recorders (all but instrument 6). The analysis extends to twice the peak frequency.

The results of this analysis are summarized in Figs. 7–9. Figures 7 and 8 show the reconstruction of two whitecap events, one associated with relatively large partial acceleration and relatively congruent with the acceleration topography, the other with a somewhat smaller partial acceleration and less congruent with the acceleration topography. In all cases the whitecap event is close to a maximum in the partial downward acceleration; only rarely does it sit directly on top of this maximum. The acceleration level varies between $-0.05g$ and $0.35g$. Figure 9 shows the corresponding probability density for finding a given contribution to the downward acceleration at a point of breaking water.

The relatively low and variable values of downward acceleration in the reconstructed events and the lack of a better match between whitecap geometry and acceleration topography are not necessarily inconsistent with the threshold model. For various reasons, discussed previously, present computations are restricted to frequencies less than twice the peak frequency. It is to be expected that the higher frequencies will also contribute significantly to the acceleration field. We have argued that the horizontal scale of this contribution should be relatively small; nonetheless, this scale is not necessarily small compared with the scale of the whitecaps included in the reconstruction

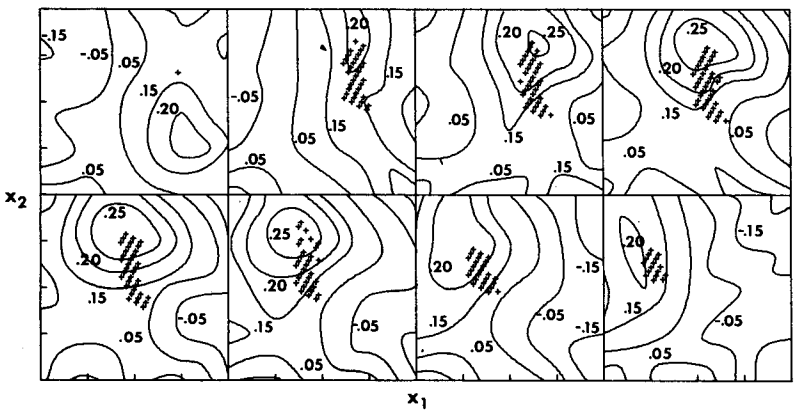

FIG. 8. As in Fig. 7 but for Event 78, film 9, 1972.

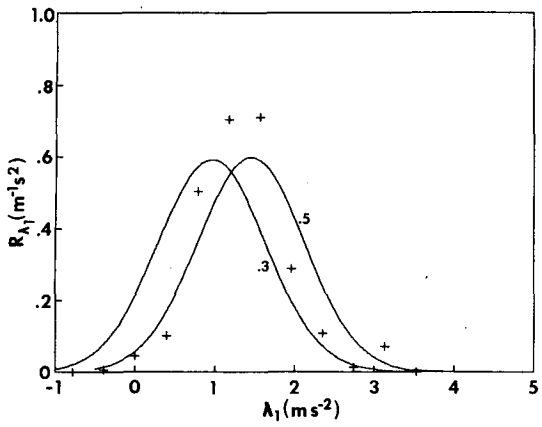

FIG. 9. Probability of finding partial acceleration level in unit area of breaking water. Crosses are experimentally determined estimates derived from reconstruction analysis. Curves are predictions of threshold model for $\Lambda_c/g = 0.3$ and 0.5, assuming $N = 5$.

analysis (essentially all whitecaps occurring in the vicinity of the wave staffs). Thus the higher frequencies may well be important to understanding the results of this analysis.

To better assess whether the reconstruction analysis is or is not consistent with the threshold model, we attempt to simulate the probability density of Fig. 9 from the threshold model. Consistent with our best guess as to its effective value during the experiments (based on the ratio between the linear size of the largest and smallest whitecaps photographed) we set $N = 5$ and represent λ in the form

$$\lambda = \lambda_1 + \lambda_2 + \lambda_3 + \lambda_4,$$

where λ_1 is the contribution to λ of wave components in the frequency range 0 to 2Ω and λ_n is the contribution in the range $n\Omega$ to $(n+1)\Omega$, $n > 1$. The λ_n are presumably independent Gaussian variables with the joint probability density

$$P_{\lambda^4}(\lambda_1, \lambda_2, \lambda_3, \lambda_4) = \frac{1}{(2\pi)^2} \frac{1}{(\sigma_1\sigma_2\sigma_3\sigma_4)} \exp\left[-\frac{1}{2}\sum_n^4 \frac{\lambda_n^2}{\sigma_n^2}\right]$$

where the covariances σ_n^2 are approximated by (Kennedy, 1978)

$$\sigma_n^2 = \alpha g^2[\ln(n+1) - \ln n], \quad n = 1, 2, 3, 4. \quad (2)$$

The probability that λ_1, λ_2, λ_3, and λ_4, chosen at random, will have a sum

$$\lambda_1 + \lambda_2 + \lambda_3 + \lambda_4 \geq \Lambda_c$$

is given by the integral

$$Q = \int_{-\infty}^{\infty} d\lambda_1 \int_{-\infty}^{\infty} d\lambda_2 \int_{-\infty}^{\infty} d\lambda_3 \times \int_{\Lambda_c-\lambda_1-\lambda_2-\lambda_3}^{\infty} d\lambda_4 P_{\lambda^4}(\lambda_1, \lambda_2, \lambda_3, \lambda_4).$$

Thus the conditional probability density $R_{\lambda_1}(\lambda_1)$ for λ_1, given

$$\lambda_1 + \lambda_2 + \lambda_3 + \lambda_4 \geq \Lambda_c,$$

is

$$R_{\lambda_1}(\lambda_1) = \frac{1}{Q}\int_{-\infty}^{\infty} d\lambda_2 \int_{-\infty}^{\infty} d\lambda_3 \times \int_{\Lambda_c-\lambda_1-\lambda_2-\lambda_3}^{\infty} d\lambda_4 P_{\lambda^4}(\lambda_1, \lambda_2, \lambda_3, \lambda_4).$$

This integral is shown as a function of λ_1 in Fig. 9 for $\Lambda_c/g = 0.3$ and $\Lambda_c/g = 0.5$.

Clearly the computed probability densities bear a remarkable resemblance to the observed density, with the $\Lambda_c/g = 0.5$ curve fitting the data somewhat better than the $\lambda_c/g = 0.3$ curve. We feel that this comparison is significant if somewhat indirect evidence for a vertical acceleration threshold of approximately $0.5g$.

6. Observed statistics

In the previous section we discussed the relatively direct comparison between experiment and theory provided by the estimation of partial acceleration levels in selected whitecaps. In this section we discuss the less direct but equally important comparison between observed and predicted whitecap statistics. This comparison is in several parts. We begin by estimating the fundamental statistic $Q_1^{(1)}$, the probability of breaking. We then examine several lower order geometrical moments and the statistic $R_2^{(2)}$ for runs 13, 14, and 15, from December 1972. Finally we estimate some average moments and moment probability densities for all runs.

An important element in the computation of geometrical moments is the estimation of a point of initial breaking for each complete whitecap event (an event which begins and ends within the field-of-view of the camera). There are two problems in determining this point, one experimental and the other philosophical. The first is that the photographic record does not explicitly contain any points of initial breaking (because it is discrete). The second is the expectation that a given event may have more than one such point. Our solution to both problems is simple, but it introduces an obvious bias into the moment computations. Because we can practically resolve only the first point of initial breaking associated with a given event, we choose to base our moment computations on this point. We determine this point by linear extrapolation from the first two recorded frames in the event, assuming that the time of initial breaking is approximately one frame interval prior to the first frame (i.e., that the lag time for the camera startup is comparable with a frame interval). We note that a similar (but not identical) prescription was followed in reducing the Monte Carlo simulations of

Part II, so that the results of these two analyses are comparable. The resulting moment statistics are not, however, directly comparable to moment statistics derived from the breaking variable probability densities of type 2 defined in Part I (because of the bias inherent in employing only first points of initial breaking).

The mechanics of collating the various statistics from the digital images of whitecap photographs will not be described here. This collation was tedious (even with the computer) but essentially straightforward.

Using all recorded events, complete and incomplete, the probability of breaking $Q_1^{(1)}$ was estimated for each run. This statistic is included in Table 2 and is shown in Fig. 10 plotted against the contribution to λ_1 rms from Eq. (1) of Part I for $\Lambda_c/g = 0.5$. Two curves are included in the figure. The solid curve is based on the assumption that the full spectrum cuts off at 2Ω (i.e., is identical with the observed spectrum), the dashed curve on the assumption that this spectrum cuts off at 5Ω. In this case we assume that the contribution to λ rms from frequencies between 2Ω and 5Ω is consistent with Eq. (2). As in Fig. 9, this comparison supports the threshold model with $\Lambda_c/g \approx 0.5g$ (assuming an effective high frequency cutoff of approximately five times the peak frequency).

Figures 11–16 show several lower order moments and moment statistics for all complete events in runs 13, 14, and 15. Figures 11–13 show the moments $M_{00}(\tau)$, $M_{10}(\tau)$, and $M_{01}(\tau)$; the latter two moments have been rotated so that the x_1 axis is downwave (in the direction Θ) and the x_2 axis is crosswave. Note that the downwave moment typically reflects the same patch velocity as the simulations of Part II, i.e., approximately one half the crest velocity defined by the peak frequency Ω. Figures 11–13 should be compared with similar figures in Part II.

Figure 14 shows the downwave moment $M_{10}(\tau)$ for all secondary group events in runs 13, 14, 15. Each secondary event has been translated so that the corresponding primary event starts at the origin. Com-

TABLE 2. Moment statistics.

Run	Ω	$Q_1^{(1)}$ (10^{-3})	Number of events	Number of complete events	$\langle M_{000}\rangle$ (m^2 s)	$\langle M_{001}\rangle$ (m^2 s^2)	$\langle M_{010}\rangle$ (m^3 s)	$\langle M_{100}\rangle$ (m^3 s)	$\langle M_{00}\rangle$ (m^2)	$\langle M_0\rangle$ (s)	$\langle T\rangle$ (s)	$\langle A\rangle$ (m^2)	Number of events/area/time (10^{-3} m^{-2} s^{-1})	Number of events/area (10^{-3} m^{-2})
4–5	2.58	0.224	141	79	0.219	0.098	−0.020	−0.121	0.383	0.170	0.514	1.162	1.022	0.585
6–7	2.47	0.259	150	82	0.238	0.136	−0.027	−0.277	0.371	0.165	0.509	1.225	1.088	0.698
8–9	2.37	0.615	94	62	0.730	0.600	−0.104	−1.141	0.648	0.211	0.938	3.025	0.842	0.949
45–46	2.15	0	0	0									0	0
51–52	2.17	0	0	0									0	0
53	2.65	0.181	178	127	0.283	0.154	0.092	−0.238	0.441	0.172	0.496	1.390	0.640	0.410
55	2.71	0.112	95	73	0.132	0.051	0.007	−0.089	0.259	0.150	0.450	0.863	0.848	0.432
56	2.18	0.393	168	135	0.326	0.216	0.291	−0.298	0.405	0.195	0.628	1.387	1.205	0.970
57	2.16	0.024	43	34	0.276	0.131	0.193	−0.087	0.515	0.194	0.438	1.221	0.086	0.046
58–59	2.38	0.216	174	114	0.219	0.100	0.137	−0.062	0.395	0.183	0.476	1.065	0.986	0.546
60–61	2.24	0.104	148	129	0.340	0.183	0.272	−0.083	0.495	0.227	0.629	1.394	0.305	0.210
62	2.42	0.279	200	160	0.349	0.187	0.257	0.105	0.505	0.215	0.614	1.456	0.799	0.552
3	2.45	0.148	124	78	0.199	0.077	−0.021	−0.125	0.400	0.177	0.409	1.000	0.743	0.370
4	2.63	0.070	38	27	0.211	0.102	−0.032	−0.193	0.365	0.171	0.431	1.045	0.331	0.191
5	2.45	0.188	86	53	0.108	0.040	−0.009	−0.088	0.220	0.141	0.446	0.750	1.741	0.854
6	2.35	0.186	53	38	0.183	0.100	0.007	−0.254	0.272	0.151	0.461	1.090	1.016	0.683
7	2.38	0.167	66	46	0.077	0.023	−0.015	−0.038	0.184	0.144	0.380	0.518	2.168	0.907
8	2.51	0.286	60	33	0.130	0.051	−0.033	−0.107	0.220	0.139	0.511	0.916	2.200	1.300
13	2.30	0.380	51	28	0.167	0.064	0.067	−0.102	0.301	0.154	0.496	1.055	2.275	1.262
14	2.19	0.320	45	27	0.188	0.081	0.053	−0.156	0.305	0.164	0.537	1.077	1.702	1.049
15	2.08	0.556	22	10	0.375	0.257	0.341	−0.527	0.437	0.152	0.563	2.226	1.482	1.272
26	2.41	0.130	46	30	0.175	0.076	0.018	−0.154	0.284	0.149	0.483	1.080	0.743	0.457
27	2.42	0.255	43	20	0.266	0.146	−0.064	−0.282	0.306	0.151	0.713	1.550	0.958	0.833
28	2.45	0.163	62	37	0.159	0.080	0.011	−0.166	0.278	0.145	0.483	1.016	1.025	0.586
29	2.13	0.486	57	22	0.133	0.054	0.028	−0.113	0.248	0.142	0.460	0.875	3.654	1.959
30	2.02	0.303	30	11	0.113	0.057	−0.049	−0.132	0.157	0.131	0.545	0.821	2.681	1.929
31	2.36	0.024	12	7	0.064	0.027	0.036	−0.058	0.105	0.130	0.393	0.454	0.375	0.228
32	2.36	0.008	2	2	0.295	0.100	0.104	−0.160	0.537	0.191	0.563	1.563	0.027	0.014
33	2.60	0.039	10	8	0.371	0.173	0.137	−0.415	0.568	0.183	0.578	1.924	0.105	0.068
34	2.60	0.102	26	16	0.166	0.063	−0.014	−0.116	0.292	0.143	0.516	1.130	0.614	0.349
35	2.56	0.183	45	28	0.148	0.052	0.001	−0.100	0.277	0.152	0.460	0.905	1.236	0.660
36	2.55	0.085	23	14	0.187	0.074	0.089	−0.164	0.294	0.142	0.500	1.181	0.454	0.289
			2292											

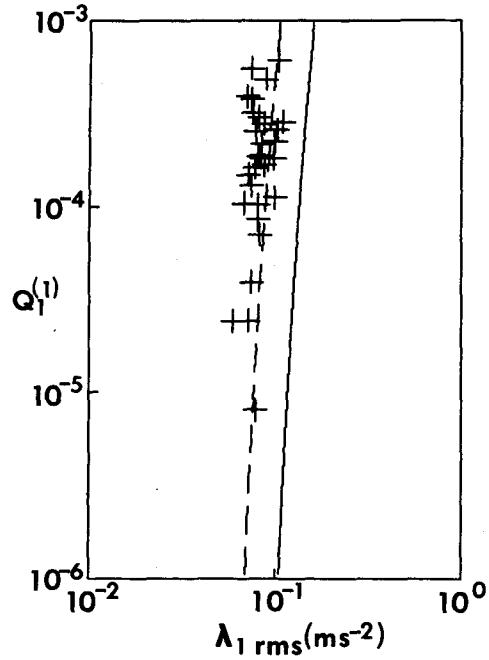

FIG. 10. Probability of breaking as a function of rms partial acceleration; threshold model prediction, $N = 2$ (solid line) and $N = 5$ (dashed line). Crosses are experimental data.

parison with Figure 10 of Part I corroborates the speculation that the secondary ridge in the Part I figure is due to secondary group events occurring on the wave crests succeeding the primary event. This comparison also suggests that secondary events also contribute to the primary ridge in this figure (probably the result of intermittent breaking on the primary wave crest).

Figures 15 and 16 show the resulting estimates for the statistics $\langle M_0(\xi)\rangle$ and $R_2^{(2)}(\xi, \tau)$. In these figures the horizontal coordinates retain their compass orientations (the x_1 axis points east).

Figures 17 and 18 summarize the mean moments $\langle M_{00}(\tau)\rangle$, $\langle M_{10}(\tau)\rangle$, and $\langle M_{01}(\tau)\rangle$ (complete events)

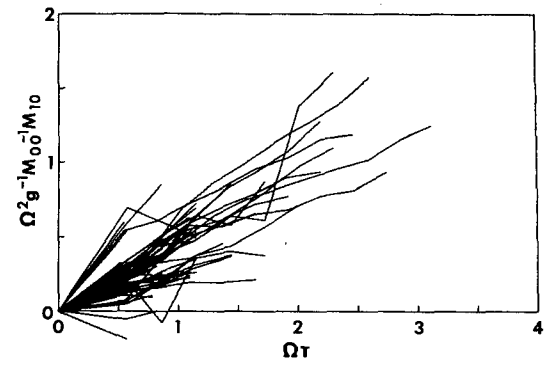

FIG. 12. Downwave center of gravity. All complete events, runs 13, 14, 15, 1972.

for all runs from the 1968 and 1972 experiments, respectively. Note the similarity between these moments and those presented for somewhat different directional spectra in Part II.

Finally Figs. 19 and 20 summarize the corresponding probability densities for the moments M_{000} and M_{001} and for the parameters A and T. The mean moments $\langle M_{000}\rangle$, $\langle M_{001}\rangle$, $\langle M_{010}\rangle$, $\langle M_{100}\rangle$, $\langle M_{00}\rangle$, $\langle M_0\rangle$, $\langle \mathrm{T}\rangle$ and $\langle A\rangle$ are tabulated in Table 2.

It should be noted that the above moment statistics are presumably functions of the "effective" cutoff parameter N. In the present case this parameter is believed to be in the range $N = 5$ to $N = 10$.

The authors regret that an experimental determination of the conditional probability $R_2^{(1)}(\xi, \tau)$ was not attempted. The information necessary to make this determination is contained in the whitecap photographs, but we did not fully appreciate the value of this determination until too late (when a lack of resources and the pressure of other matters prevented our carrying out the necessary computation).

7. Conclusions

Despite our inability to deal directly with higher frequency wave components, we have carried forward

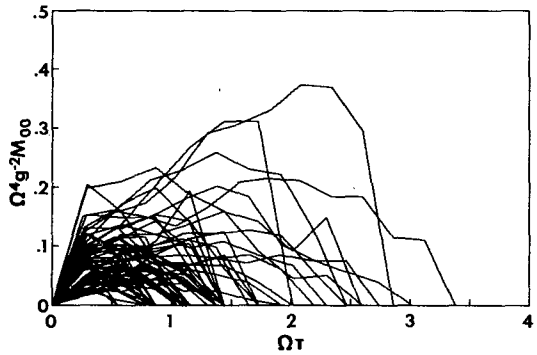

FIG. 11. The $M_{00}(\tau)$. All complete events, runs 13, 14, 15, 1972.

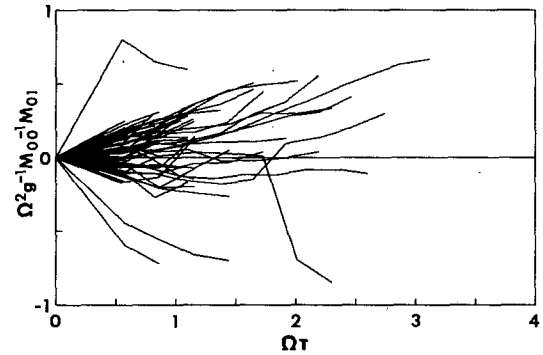

FIG. 13. Crosswave center of gravity. All complete events, runs 13, 14, 15, 1972.

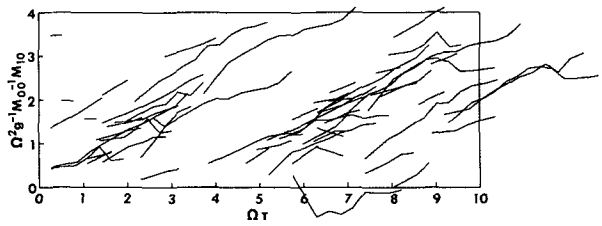

FIG. 14. Downwave center of gravity. All secondary units. Runs 13, 14, 15. Primary events (not shown) start at origin.

an extensive and comprehensive evaluation of the hypothesis that for light-to-moderate winds waves break when the (negative) vertical acceleration exceeds one half the acceleration of gravity. Our investigation has proceeded on several fronts. After defining the terms of reference for the investigation, we examined several theoretical predictions of the threshold model, estimating whitecap statistics by direct integration of the joint probability densities for the threshold variable field and by Monte Carlo simulation of the breaking variable field. At the same time we carried out a field experiment designed to test these theoretical predictions. The comparison between theory and experiment is essentially supportive of the threshold hypothesis. We find

1) "Partial" acceleration levels estimated from the wave records ($0 - 2\Omega$) range from $-0.05g$ to $0.35g$ with a mean of $\sim 0.14g$. The statistical distribution of these levels is consistent with a critical level of $\sim 0.5g$, assuming that the "effective" spectrum producing the observed whitecaps goes as ω^{-5} between 2Ω and 5Ω cutting off at 5Ω, and assuming that the contribution to the acceleration from different frequency bands is statistically independent.

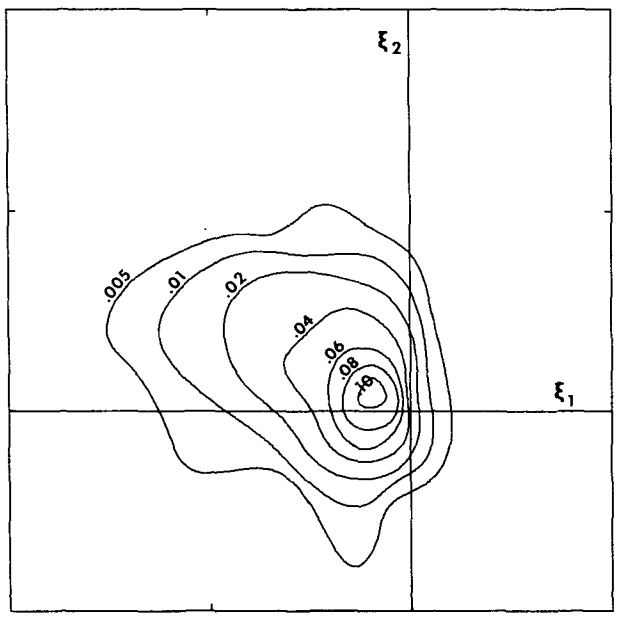

FIG. 15. $\langle M_0(\xi) \rangle$. Runs 13, 14, 15. Horizontal scale is 2 m per division. Contours in s.

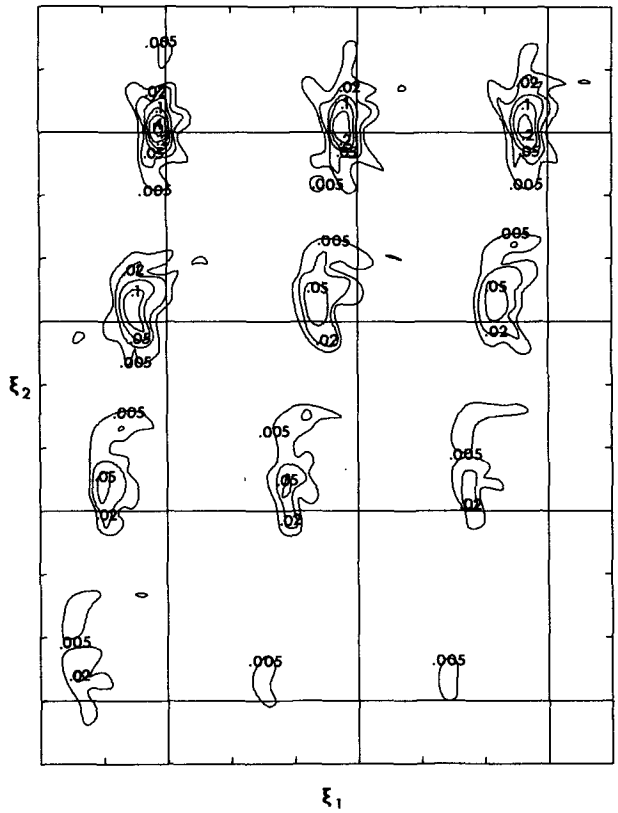

FIG. 16. $R_2^{(2)}(\xi, \tau)$. Runs 13, 14, 15. Shown in increments of 0.125 s starting at upper left. Sequence runs from top to bottom, left to right. Horizontal scale is 2 m per division.

2) The probability of breaking $Q_1^{(1)}$ is well correlated with the rms partial acceleration. This correlation is well predicted by theory [making the same allowance for higher frequency wave components as in 1)].

3) The data confirm that, as implied by Fig. 10 of Part I, the breaking of a given wave crest increases the probability that, at a point two wavelengths downwave and at a time one wave period later, the succeeding wave crest will also break. The relevant frequency scale is generally significantly larger than the peak frequency Ω.

4) The moments $M_{00}(\tau)$, $M_{10}(\tau)$, and $M_{01}(\tau)$ for individual whitecap events are comparable with moments resulting from the Monte Carlo simulations of Part II. In agreement with these simulations, whitecaps move downwave at a speed which is significantly smaller than the phase speed of the dominant wave component (typically 0.5 this speed), emphasizing the importance of higher frequency wave components to the breaking process.

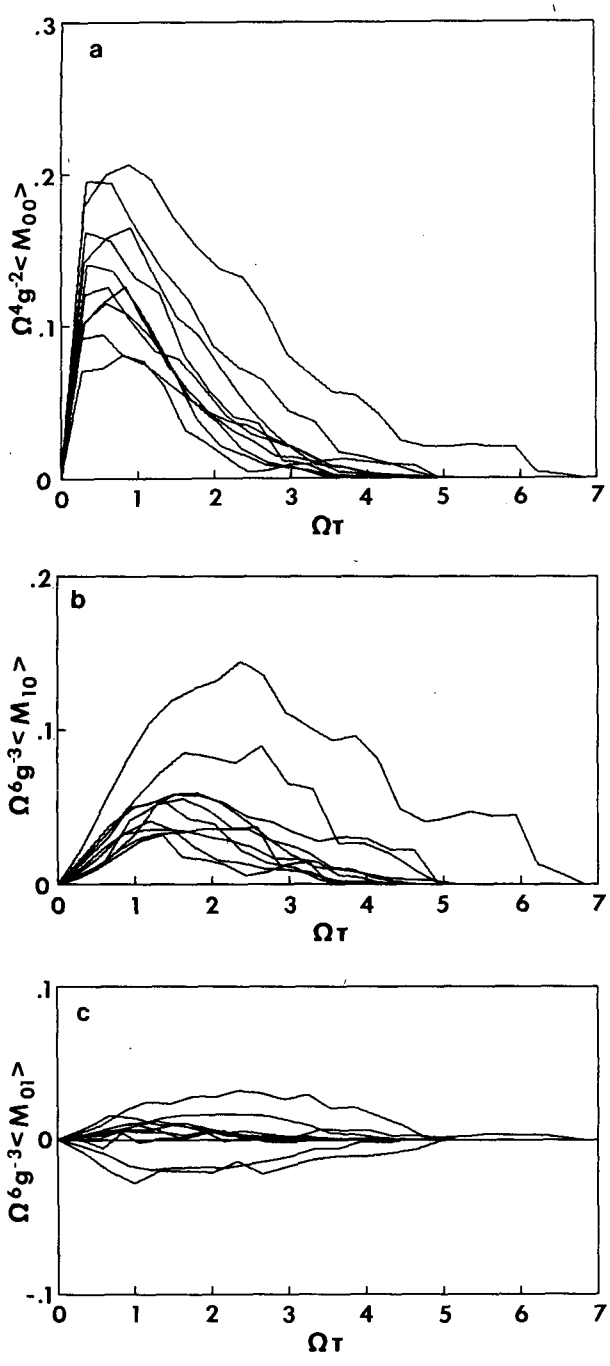

FIG. 17. Average moment statistics for (a) $\langle M_{00} \rangle$, (b) $\langle M_{10} \rangle$ and (c) $\langle M_{01} \rangle$, April 1968. Statistics shown run by run. ξ_1 axis downwave.

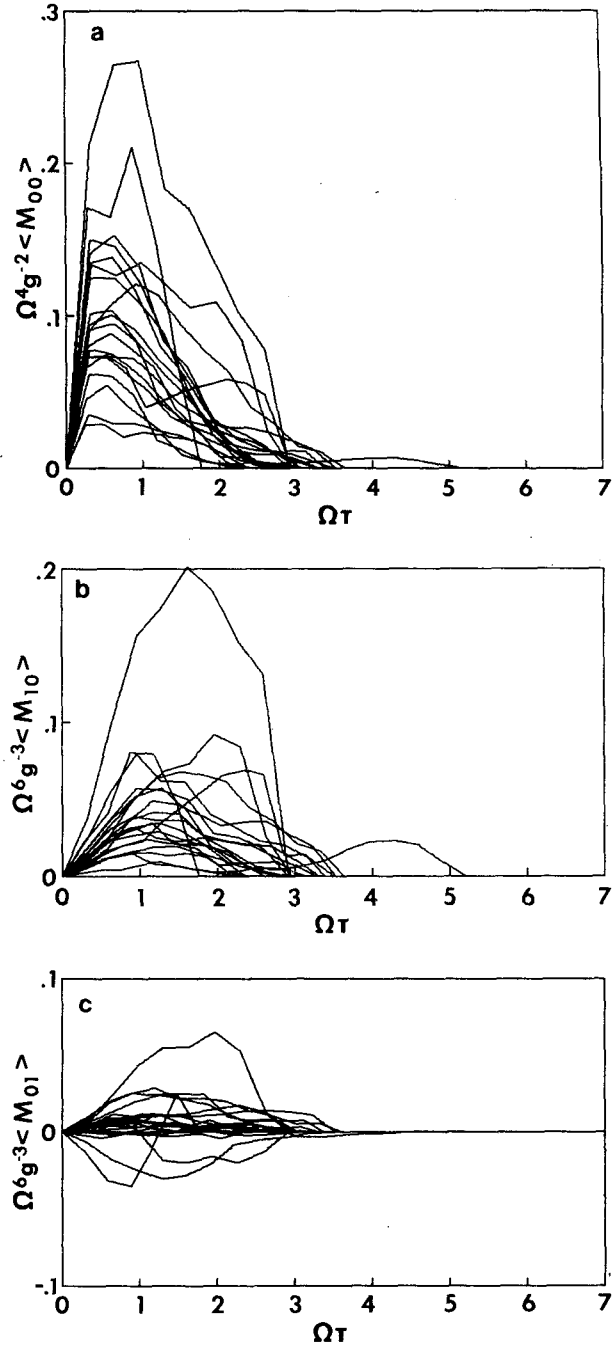

FIG. 18. As in Fig. 17 but for December 1972.

5) Comparison of various mean moments with those computed from the Monte Carlo simulations of Part II suggests a broad range of both quantitative and qualitative agreement.

We believe that these findings, while not conclusive, suggest strongly that the vertical acceleration criterion may very well be an acceptable practical predictor of whitecap events and that linear wave theory may be an acceptable framework for the application of this criterion. However complex the dynamics of the breaking mechanism may be, there appears nonetheless to be a comparatively simple level of description which successfully accounts for the lower order geometry and statistics of the whitecap field.

Our investigation supports a (negative) vertical acceleration threshold of approximately $0.5g$. While the

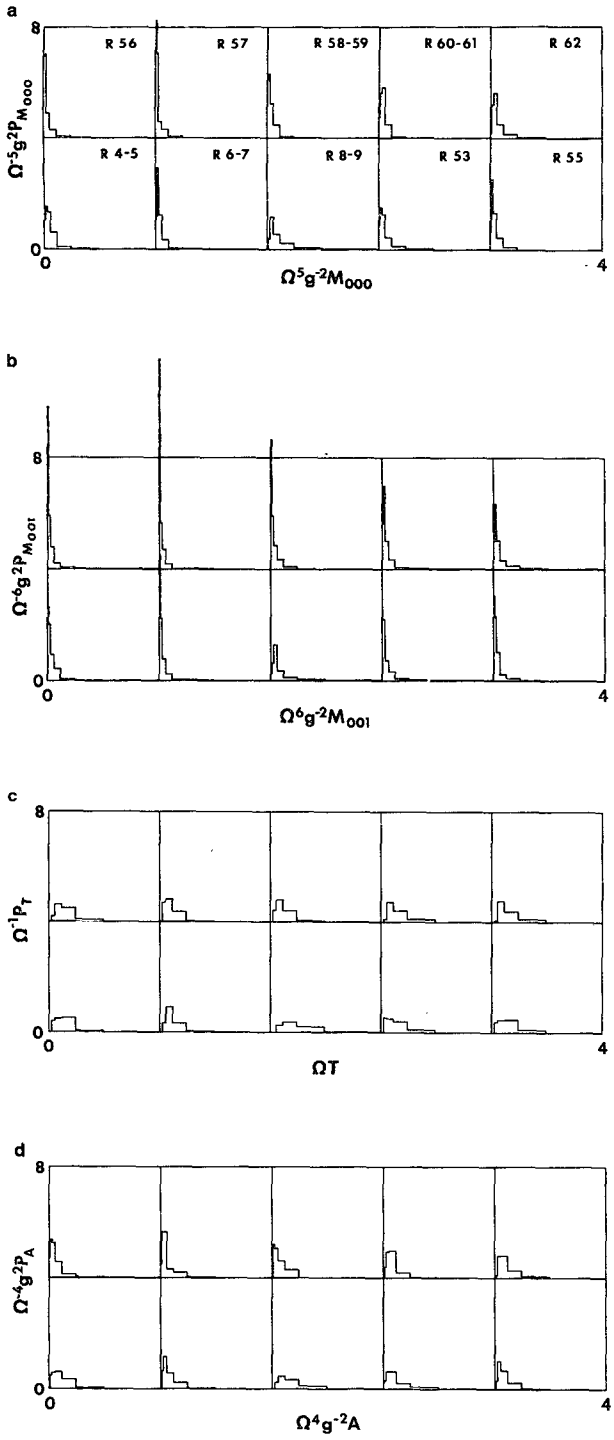

FIG. 19. Moment probability densities for (a) M_{000}, (b) M_{001}, (c) T and (d) A, April 1968.

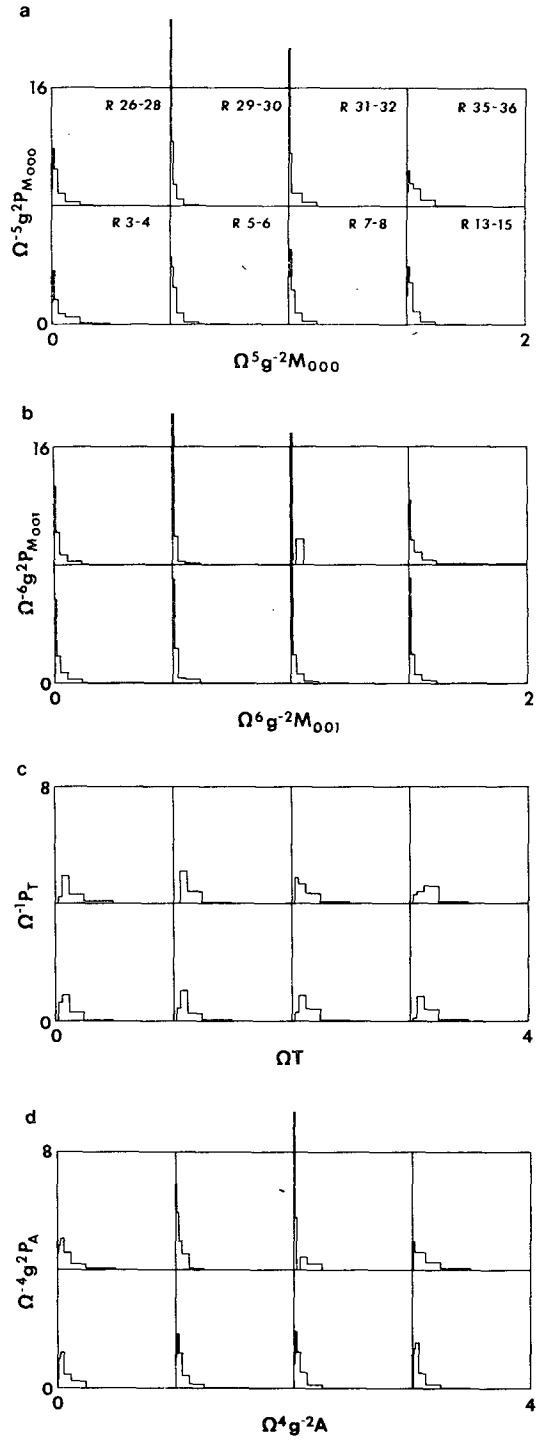

FIG. 20. As in Fig. 19 but for December 1972.

model is quite sensitive to this threshold, our inability to monitor higher frequency wave components prevents a more precise determination of it. We speculate that in fact the threshold appropriate to the linear part of the (negative) vertical acceleration field is probably something less than $0.5g$, consistent with a threshold of $0.5g$ for the full field. As in the case of the Stokes wave, nonlinear "forced" components might be expected to account for approximately 10% of the full breaking field. We anticipate that these

nonlinear components may well be crucial to understanding the higher order geometry of whitecaps. We believe, however, that their impact on the lower order geometry described in this study is minimal.

Our study was conceived with the rather limited objective of evaluating the threshold hypothesis and developing a description of the lower order geometrical and geometrostatistical properties of whitecaps. We have made no attempt to describe the small scale motions within a whitecap. We also have made no attempt to estimate the energy and momentum transfer to and/or from wave components resulting from the whitecapping process.

This latter estimate, which is necessary to understanding the growth and decay of the wave spectrum, may or may not be developable in part from the geometrical description contained in this study. If so, one approach to this estimate would be 1) to discover appropriate algorithms relating the total energy and momentum transfer to some geometrostatistical property and 2) to discover appropriate algorithms for partitioning this transfer among the various wave components.

Hasselmann (1974) suggests that the energy transfer from whitecapping is in fact everywhere negative and is partitioned in direct proportion to the spectral intensity of a given wave component and to the square of its frequency. This result is independent of the precise nature of the breaking process, so long as it is weak in the mean (contributing "slowly" to the evolution of the spectrum).

What remains is to fix the total energy transfer and with it Hasselmann's undertermined constant of proportionality. Intuitively one might expect this transfer to be roughly proportional to the product of two factors, one representing the mean spatial volume of breaking per unit area of sea surface, and a second representing the mean turbulent intensity of the breaking water. The first factor is probably obtainable from the threshold model, the second is probably not.

Acknowledgments. Support for this work has been provided by ONR Contract N00014-67-A-0386-0001 and NSF Grant-in-Aid OCE76-10739.

We thank Commander Dickinson of the R/V *Gerda* for his able boat handling and cooperative spirit during the early phases of the field work. Willie Campbell of the R/V *Gulfstream* skippered the final cruise. Dave Hunley made innumerable contributions to the technical side of the work, and Norman Pflaum, Gary Davis, and Jay Hanson assisted in one way or another.

REFERENCES

Bartlett, M. S., 1950: Periodogram analysis and continuous spectra. *Biometrika,* **37,** 1–16.

Hasselmann, K., 1974: On the spectral dissipation of ocean waves due to whitecapping. *Bound.-Layer Meteor.,* **6,** 107–127.

——, T. P. Barnett, E. Bouws, H. Carlson, D. E. Cartwright, K. Enke, J. A. Ewing, H. Grenapp, D. E. Hasselmann, P. Krusemann, A. Meerburg, P. Muller, D. J. Olbers, K. Richter, W. Sell and H. Walden, 1973: Measurements of wind-wave growth and swell decay during the Joint North Sea Wave Project (JONSWAP). *Erganz. Dtsch. Hydrogr. Z.,* Reihe A**8,** No. 12.

Kennedy, R. M., 1978: A probabilistic description of deep water whitecaps. Ph.D. thesis, Nova University, Fort Lauderdale, FL.

Snyder, R. L., 1974: A field study of wave-induced atmospheric pressure fluctuations above surface gravity waves. *J. Mar. Res.,* **32,** 497–531.

——, and L. Smith, 1973: On the estimation of surface gravity wave fields in the vicinity of an array of wave recorders. *J. Mar. Res.,* **31,** 51–60.

——, F. W. Dobson, J. A. Elliott and R. B. Long, 1981: Array measurements of atmospheric pressure fluctuations above surface gravity waves. *J. Fluid Mech.,* **102,** 1–59.